

<sup>1</sup>

José D. Ruiz-Álvarez

<sup>2</sup>

Compiled on 18/01/2015 at 01:53



## <sup>3</sup> Chapter 1

# <sup>4</sup> The CMS experiment at LHC

<sup>5</sup> The CMS experiment is one of the biggest particle physics experiments on the world. It  
<sup>6</sup> is located at the ring of the LHC that is the main experience managed by CERN, the  
<sup>7</sup> European Organization for Nuclear Research or Centre Européenne pour la Recherche  
<sup>8</sup> Nucléaire by its name on french. This center constitutes the biggest center for research  
<sup>9</sup> on particle physics all over the world. All along its 60 years of existence, from 1954,  
<sup>10</sup> 21 member states have been joining it, but an overall of 113 countries participate in  
<sup>11</sup> different ways on this center.

<sup>12</sup> On the present chapter we discuss in detail different aspects of the LHC accelerator  
<sup>13</sup> and the CMS experiment. In particular we make some emphasis in the CMS sub-  
<sup>14</sup> detectors related to jets, objects that play the main role on the search that is the main  
<sup>15</sup> subject of the present work. We also discuss the present state of both machines, their  
<sup>16</sup> achievements and the challenges that were came through. Finally, also the expectations  
<sup>17</sup> and goals for the upcoming run II are mentioned.

### <sup>18</sup> 1.1 The Large Hadron Collider

<sup>19</sup> The Large Hadron Collider, or LHC [1], is a machine that accelerates and collides protons  
<sup>20</sup> and heavy ions. This machine is the biggest particle collider nowadays with a circumfer-  
<sup>21</sup> ence of 27 km. It also achieves the greatest energy by a collider up to present, planned  
<sup>22</sup> to be 14 TeV at the center of mass of the collision. On the first run of the machine  
<sup>23</sup> only 8 TeV were achieved, and next run is planned to start with 13 TeV. It's located  
<sup>24</sup> in French-Swiss border near to Geneva. The tunnel for the machine was carved around  
<sup>25</sup> 100 m under the ground, 45 m under the Jura mountains and 170 m under the Léman  
<sup>26</sup> lake with an inclination of around 1.4%, sloping down towards the lake . This machine  
<sup>27</sup> has used as much as possible old LEP buildings and sites, that was an electron-positron  
<sup>28</sup> collider built between 1984 and 1989.

<sup>29</sup> The protons and heavy ions accelerated by the machine are collided in different  
<sup>30</sup> points where dedicated experiments are located to detect and study the product from  
<sup>31</sup> the collisions. The four main experiments located on the LHC ring are CMS [2, 3],  
<sup>32</sup> ATLAS [4], LHCb [5] and ALICE [6]. The first two are experiments of generic purpose

33 where searches for new physics and also precision measurements are performed. LHCb  
 34 is dedicated to the physics of the b-quark, and ALICE focuses on the study of the  
 35 quark-gluon plasma produced from heavy ions collisions. However one of the principal  
 36 objectives of the construction of the LHC was the discovery of the Higgs boson, generic  
 37 searches on new physics have been conducted from the very beginning of the first data  
 38 taking on 2009. Moreover, after the Higgs discovery on 2012 there is a growing effort on  
 39 the searches for new physics and precision measurement on the properties of the Higgs.

40 The LHC is a complex machine composed of several parts. The two principal parts  
 41 are the injector chain and the main ring. A diagram of the whole CERN complex can  
 42 be seen in figure 1.1. The injector chain has different stages that pre-accelerate protons  
 43 and heavy ions to be injected into the main ring of LHC. In the main ring the protons  
 44 and heavy ions are fully accelerated and collided in four different points over the ring.

#### 45 1.1.1 Injector chain

46 The injector chain begins with the proton source. Protons are extracted via ionization  
 47 of Hydrogen gas in the Duoplasmatron Proton Ion Source. Such extraction is pulsed,  
 48 what makes up the first bunch structure. The extracted protons are then accelerated  
 49 to 50 MeV in the linear accelerator, Linac2, that dates from 1978. After this first stage  
 50 several steps are followed:

- 51 1. Linac2 injects proton bunches in the Proton Synchrotron Booster (PSB) where are  
 52 accelerated to 1.4 GeV.
- 53 2. From PSB, the protons are delivered to the Proton Synchrotron (PS) where they  
 54 reach an energy of 25 GeV. In the PS the bunches are also split from 6 initial  
 55 bunches to 72 spaced by 25 ns.
- 56 3. Finally, the pre-acceleration chain is finished by the SPS, Super Proton Syn-  
 57 chrotron. There the bunches are accelerated up to 450 GeV right before being  
 58 inserted to the main LHC ring.

59 The whole pre-acceleration chain has been optimized to obtain the best possible  
 60 performance on the final acceleration in the LHC main ring. All parameters are carefully  
 61 controlled, for example the number of bunches, the separation between bunches, the  
 62 separation between trains of bunches or the injection energy to each subsystem. It's also  
 63 remarkable to notice the level of control achieved in the bunches manipulation, from old  
 64 subsystems as the PS from 1959 or the newest, the SPS that dates from 1976.

65 Some recent plans for future accelerator have been theorized using the LHC main  
 66 ring as injector for a bigger accelerator, for example the so called Very Large Hadron  
 67 Collider or VLHC.

#### 68 1.1.2 Main ring

69 The main ring is composed of two rings that accelerate the proton bunches in opposite  
 70 directions, clock-wise and counter clock-wise. An schematic view of the design of the

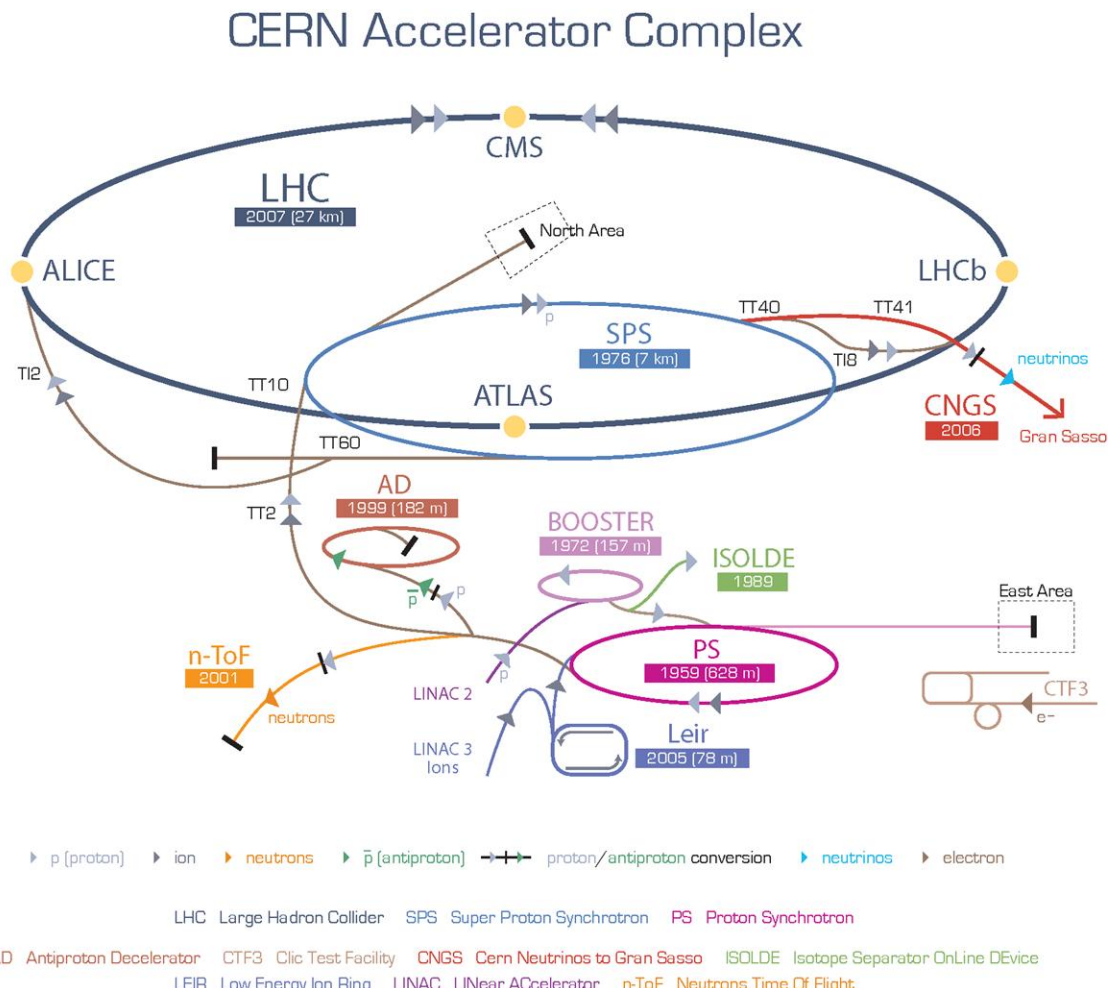


Figure 1.1: Organization of CERN complex

71 main ring can be seen in figure 1.2. The rings crosses in different points in order to collide  
 72 the protons and they are divided in eight straight sections and eight arcs. In each octant  
 73 bunches are controlled by dipole magnets. These magnets, in figure 1.3, need to produce  
 74 a very strong magnetic field in order to be able to bend a 7 TeV beam of protons. This  
 75 intense magnetic field, 8.33 T, is produced by electrical currents that are only achievable  
 76 by means of superconductivity. All the 1232 dipoles operate at a temperature of 1.9 K,  
 77 under cooling by liquid helium. They also operate under ultra-high-vacuum. The beam  
 78 lines with a pressure less than  $10^{-9}$  mbar and the whole dipole system with  $10^{-6}$  mbar,  
 79 that serves also as insulating system from the surroundings. In addition, the LHC main  
 80 ring has other magnets that focus and correct different characteristics of the beam: 520  
 81 quadrupoles, 2464 sextupoles, 1232 octupoles.

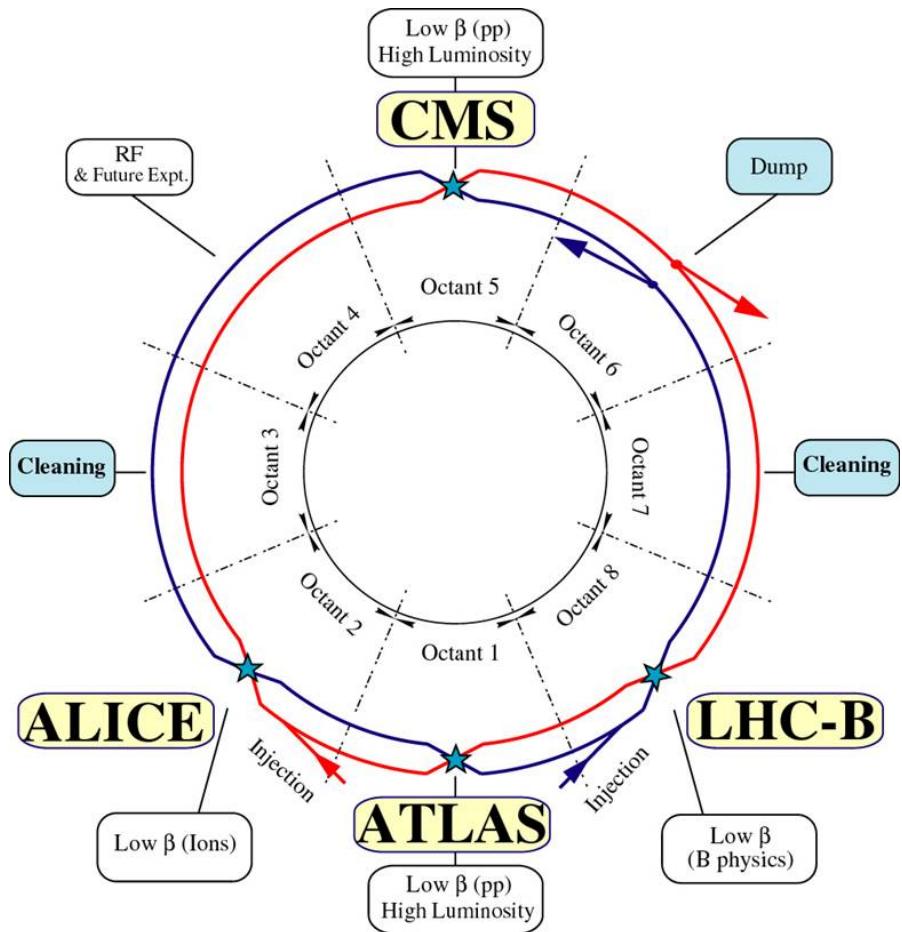


Figure 1.2: Schematic of the LHC main ring design.

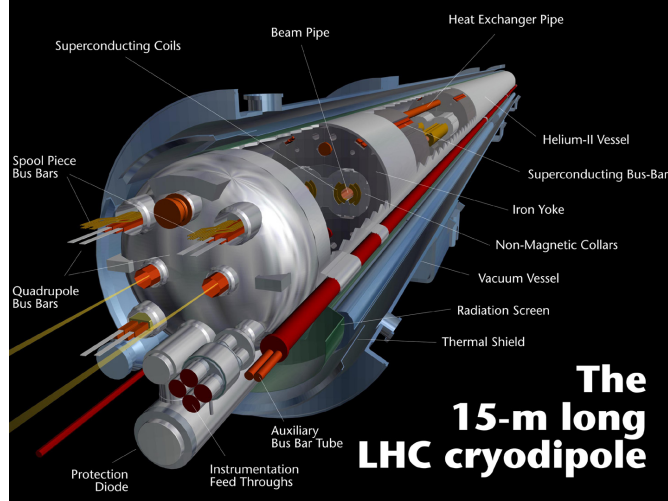


Figure 1.3: Design of LHC cryodipole that bends the beam in the main ring.

## 82 Luminosity

83 On collider physics, such as the LHC, the figure of merit is the luminosity, given in  
 84 equation 1.1. The luminosity is proportional to the number of events per second, hence  
 85 is the quantity to be maximized by the design and operation of the accelerator. In  
 86 terms of the collider characteristics depend on the number of bunches in the ring  $k_b$ , the  
 87 number of protons per bunch  $N_b$ , the revolution frequency  $f_{rev}$ , the relativistic gamma  
 88 factor  $\gamma$ , the normalized rms transverse beam emittance  $\epsilon_n$  and the beta function at  
 89 the interaction point  $\beta^*$ . The denominator on 1.1 can also be rewritten in terms of the  
 90 horizontal and vertical width of the bunches at the crossing. In table 1.1.2 can be found  
 91 the LHC beam parameters at injection and collision.

$$L = \frac{k_b N_b^2 f_{rev} \gamma}{4\pi \epsilon_n \beta^*} \quad (1.1)$$

Parameter/units	Injection	Collision
Energy [GeV]	450	7000
Luminosity [ $\text{cm}^{-2}\text{s}^{-1}$ ]		$10^{34}$
$k_b$ Number of bunches		2808
Bunch spacing [ns]		24.95
$N_b$ intensity per bunch [protons/bunch]		$1.15 \times 10^{11}$
Beam current [A]		0.58
$\epsilon_n$ normalized rms transverse beam emittance [ $\mu\text{m}$ ]	3.5	3.75
$f_{rev}$ revolution frequency [kHz]		11.25

At the crossing points, the number of events coming from collisions and produced via an specific process, is directly proportional to the luminosity provided by the collider, as in equation 1.1.

$$N_{events} = L\sigma_{process} \quad (1.2)$$

where  $\sigma_{process}$  is the cross section of the process.

The total cross section of a proton-proton collision from the crossing of two bunches at 14 TeV is 100-110 mb [7], from three different scattering processes: elastic, diffractive and inelastic. In the elastic scattering the protons only exchange momenta but their structure remain unchanged, that is the case for the majority of collisions. In diffractive scattering momenta is exchanged and also new particles are produced in addition to the two final protons. Finally, in inelastic scattering, the constituents of the protons, the partons, interchange a big amount of momentum and produce a large quantity of particles. The inelastic processes contribute less than diffraction to the total cross section. While inelastic collisions produce particles in the central rapidity (defined on 1.2.1) region, diffractive and elastic final products have a large rapidity. Only in the hard interactions, inelastic scattering, color is exchanged, being such the reason to fill up the central rapidity region.

From the crossing of two bunches not only one proton-proton interaction is expected. Around 25 interactions are expected for each crossing. From them, only one is coming from an inelastic collision, that is the type of process of more interest for detectors as CMS or ATLAS. This fact puts an additional difficulty to the detectors in order to extract the hard interaction from all the elastic and diffractive collisions happening at same time. Such phenomena is known as Pile-Up, an illustration of a collision with high pile-up can be found on figure 1.4 as seen by CMS detector.

### 1.1.3 Run 1

On February 10 of 2013 the first stable run of the LHC reached an end. This run, now called Run 1, started on November 20 of 2009. The original LHC start was planned for 2008, but an incident on one of the electric connections of one of the magnets forced to stop the 19th of September of the same year. From the restart on 2009, the energy was augmented from 450 GeV to 4 TeV per beam. The 23th of September 2009 the first collisions were detected by the experiments. One week after the achieved center of mass energy was  $\sqrt{s} = 2.36$  TeV, already more than Tevatron (1.98 TeV).

On 2010, from 30th March to 6th December 3.5 TeV per beam were reached delivering near  $50 \text{ pb}^{-1}$ . With the same energy, approximately  $6 \text{ fb}^{-1}$  were delivered on 2011.

On 2012, the center of mass energy reached one additional TeV,  $\sqrt{s} = 8$  TeV, and around  $20 \text{ fb}^{-1}$  of integrated luminosity were delivered between April and December. On figure 1.5 can be seen the progress of the recorded luminosity by CMS for 2010-2012 period. The first six weeks of 2013 were devoted to proton-lead collisions.

After this very successful run, the LHC has been stopped for a year for repair and maintenance of different systems in the experiments and in the LHC itself. After this

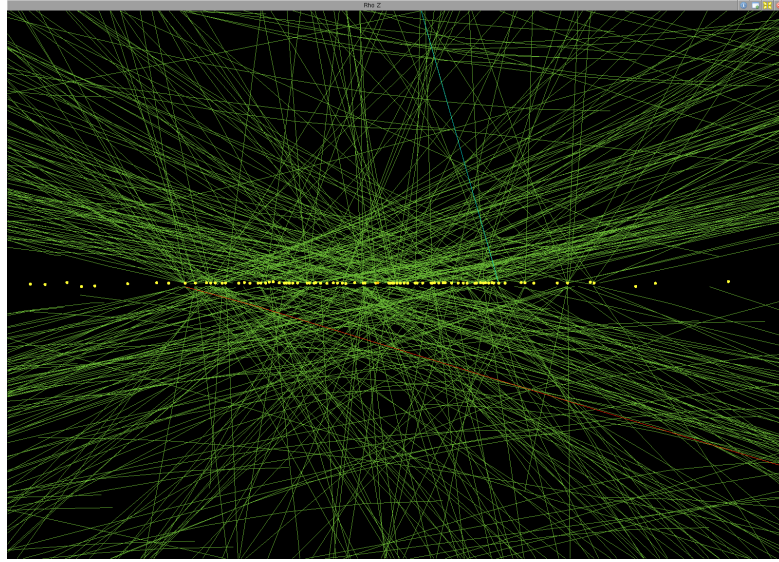


Figure 1.4: High pile-up event (78 interactions) seen by CMS detector. Event 35655522, from 198609 run, lumi 56, recorded on 2012. Image credit: Andre Holzner ©CERN

<sup>131</sup> period, known as Long Shutdown or LS1, the LHC is planned to restart a new run on  
<sup>132</sup> the early spring of 2015.

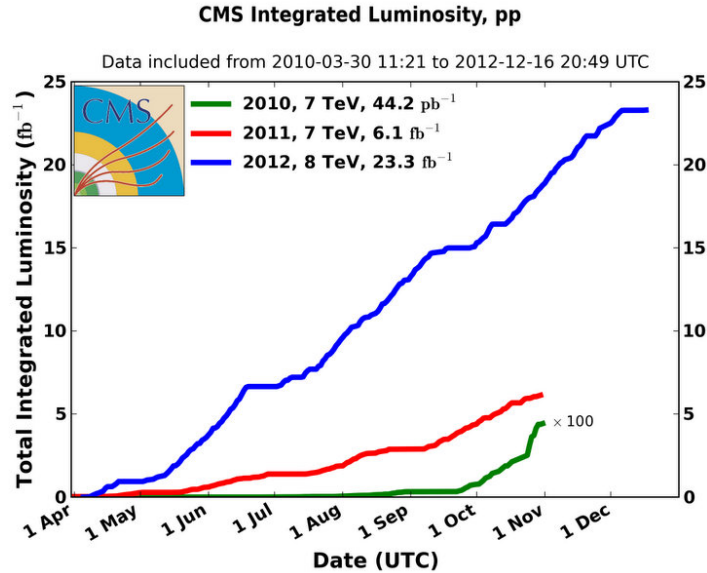


Figure 1.5: CMS integrated luminosity for proton-proton collisions delivered by LHC.  
 ©CERN

<sup>133</sup> **1.1.4 Other experiments at LHC**

<sup>134</sup> On the main ring there are several experiments depending on the collisions delivered by  
<sup>135</sup> the LHC main ring. The biggest are CMS [2] and ATLAS [4], both of them generalist  
<sup>136</sup> experiments designed to do precision measurements as well as new physics searches.  
<sup>137</sup> Mainly recording proton-proton collisions, they have also recorded ion-ion and proton-  
<sup>138</sup> ion collisions during the run 1. Both of them were designed for high instantaneous  
<sup>139</sup> luminosity,  $L = 10^{34}\text{cm}^2\text{s}^{-1}$ .

<sup>140</sup> In addition, there is other two experiments designed for specific purposes. The  
<sup>141</sup> LHCb [5] that focus on the study of the physics of the b-hadrons, specially related to the  
<sup>142</sup> CP violation, and ALICE [6] build for the study of strongly interacting matter. The first  
<sup>143</sup> of them record proton-proton collisions at an instantaneous luminosity of  $10^{32}\text{cm}^2\text{s}^{-1}$   
<sup>144</sup> and the second record ion-ion collision with  $L = 10^{27}\text{cm}^2\text{s}^{-1}$ .

<sup>145</sup> The CMS experiment is going to be described in detail on section 1.2. On the follow-  
<sup>146</sup> ing sections we are going to present very briefly the other three experiences mentioned  
<sup>147</sup> above.

<sup>148</sup> **ATLAS**

<sup>149</sup> The ATLAS experiment (A Toroidal LHC ApparatuS) is the biggest LHC experiment.  
<sup>150</sup> It's located at point one, as displayed on figure 1.2, on the LHC main ring. It's cylindrical  
<sup>151</sup> detector similar to CMS. It's about 45 meter long, 25 meter high, and weights around  
<sup>152</sup> 7000 tons. ATLAS main components are, from inside to outside, a tracking system, an  
<sup>153</sup> electromagnetic calorimeter, a hadron calorimeter and muon chambers. In between this  
<sup>154</sup> subsystems there is an internal solenoidal magnet and a set of external toroidal magnets.  
<sup>155</sup> The detector design is presented on figure 1.6.

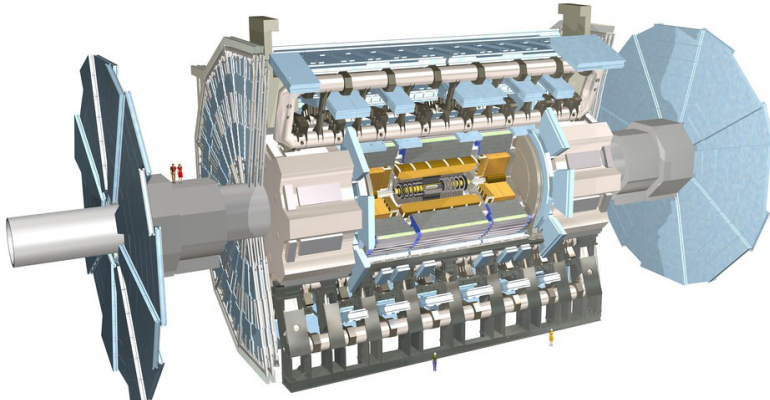


Figure 1.6: ATLAS detector internal view. ©CERN

<sup>156</sup> On the human resources side, ATLAS experiment configures a collaboration of around  
<sup>157</sup> 3000 persons, coming from 117 universities around the world, from 38 countries. A third  
<sup>158</sup> part of the collaboration are students.

159 **LHCb**

160 LHCb detector, hosted at point 8 of the LHC main ring, has a different design than CMS  
161 and ATLAS. Smaller than these, its design mainly focus to be able to detect particles  
162 produced close to the beam direction. Reason why is not cylindrically but conically  
163 shaped. It also has the same main parts, a tracking system with a very precise vertex  
164 locator, electromagnetic and hadron calorimeters, muon chambers and magnets. Its  
165 major specificity is a system that allows to distinguish different hadrons, what is crucial  
166 for the study of strong interacting matter. It measures 21 m long, 10 m high and 13 m  
167 wide, and weights 4500 tons. A view of the detector can be found on figure 1.7. The  
168 LHCb collaboration groups around 700 persons from 50 different universities over 15  
169 countries.

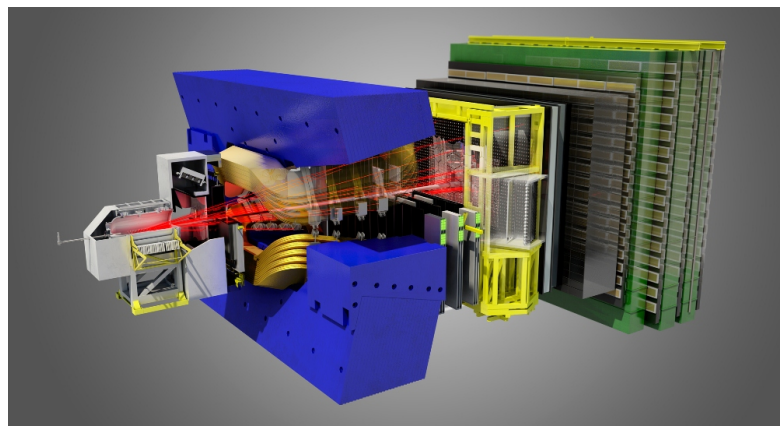


Figure 1.7: LHCb detector internal view. ©CERN

170 **ALICE**

171 The ALICE experiment (A Large Ion Collider Experiment) is located at point 2 of the  
172 LHC main ring, measures 16 m high, 16 m wide and 26 m long, and weights 10000 tons.  
173 It's an asymmetrical detector as LHCb. Its structure can be seen on figure 1.8. ALICE  
174 collaboration counts around 1500 people, from 154 physics institutes in 37 countries.

175 **1.2 The Compact Muon Solenoid experiment**

176 The CMS detector, hosted at point 5 of the LHC main ring (see figure 1.2), is the second  
177 biggest LHC experiment. Cylindrically shaped, measures 15 m of diameter and 28.7 m  
178 long, and weights 14000, making it the heaviest LHC experiment. Its subsystems are  
179 concentrically located from the collision point in the beam line. Its main characteristic  
180 is the strong 3.8 T solenoid magnet. A representation of the detector can be found in

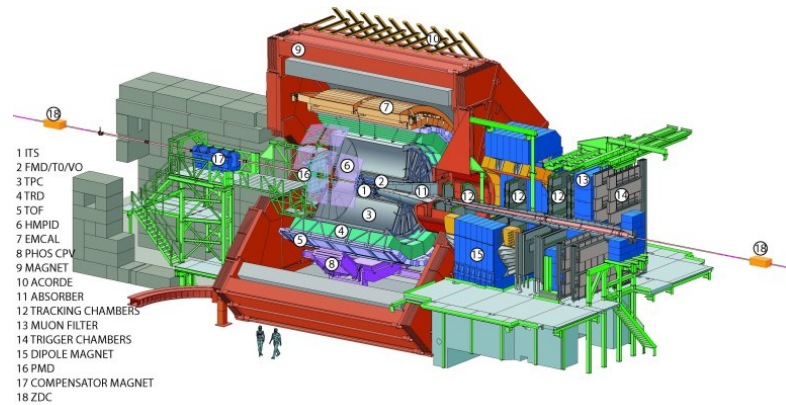


Figure 1.8: ALICE detector internal view. ©CERN

181 figure 1.9. The CMS collaboration is formed by around 2600 scientists, of which 900 are  
182 students, from 181 institutes over 41 countries.

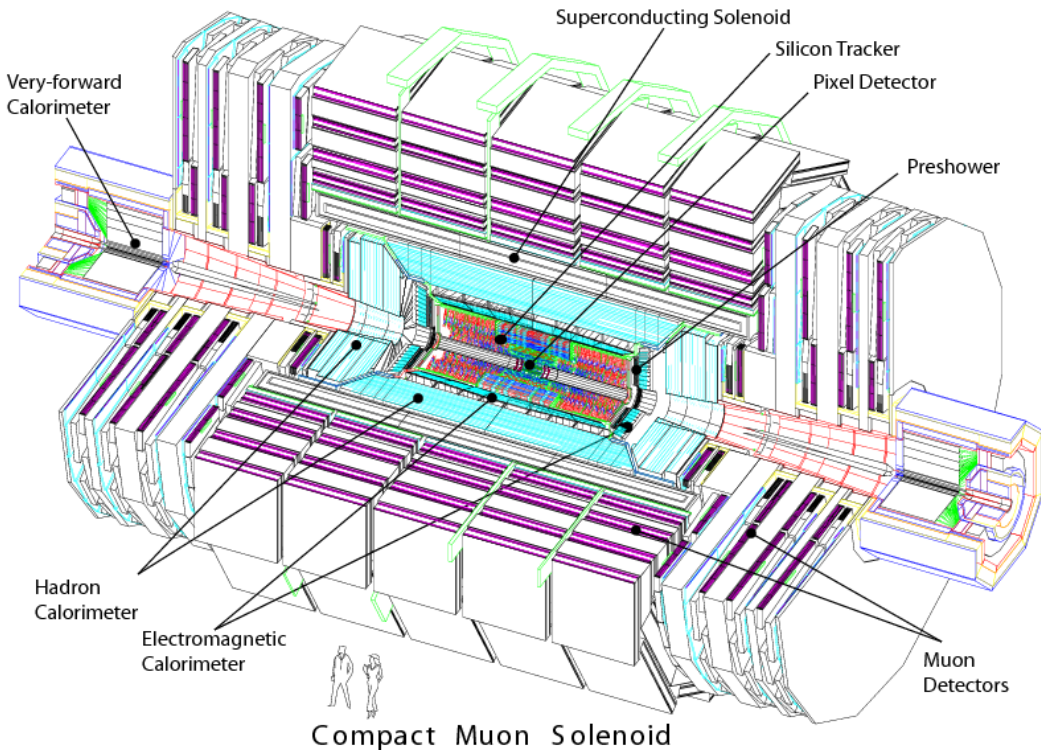


Figure 1.9: CMS detector internal view. ©CERN

CMS has been designed to be able to do very precise identification of particles originated from the collisions and their properties. For the measurement of the momentum of the charged particles, CMS counts with a very strong magnet that allows to bend very energetic particles. In addition, the calorimeters allow to measure accurately the energy from hadrons, electrons and photons. At the most external layer, the muons chambers measuring muons properties, and in the innermost the tracking system that reconstructs the collision points and the charged particles tracks. In figure 1.10 can be found a representation of the different subsystems of CMS and how particles are reconstructed from them.

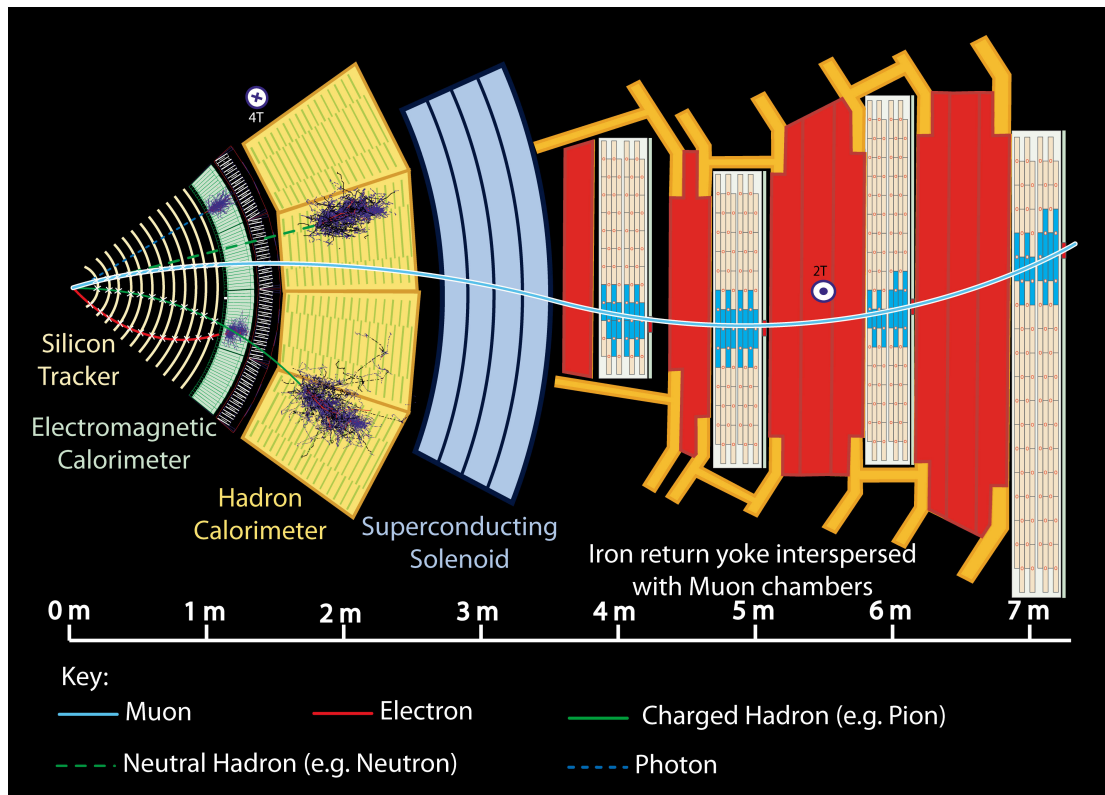


Figure 1.10: CMS sub-detectors and particle identification. ©CERN

### 1.2.1 Coordinate system

The origin of coordinates defined on the CMS detector is located on the nominal collision point, the “interaction point”. From there, the z-axis is defined along the beam pipe line pointing towards the Jura mountains. The positive/negative z-axis directions define the positive/negative sides of the detector. The y-axis is defined towards the zenith and the x-axis towards the center of the LHC plane. Due to the inclination of the LHC plane, this

198 coordinate system is slightly tilted with respect to the true vertical. A representation of  
 199 the coordinate system definition can be found in figure 1.11.

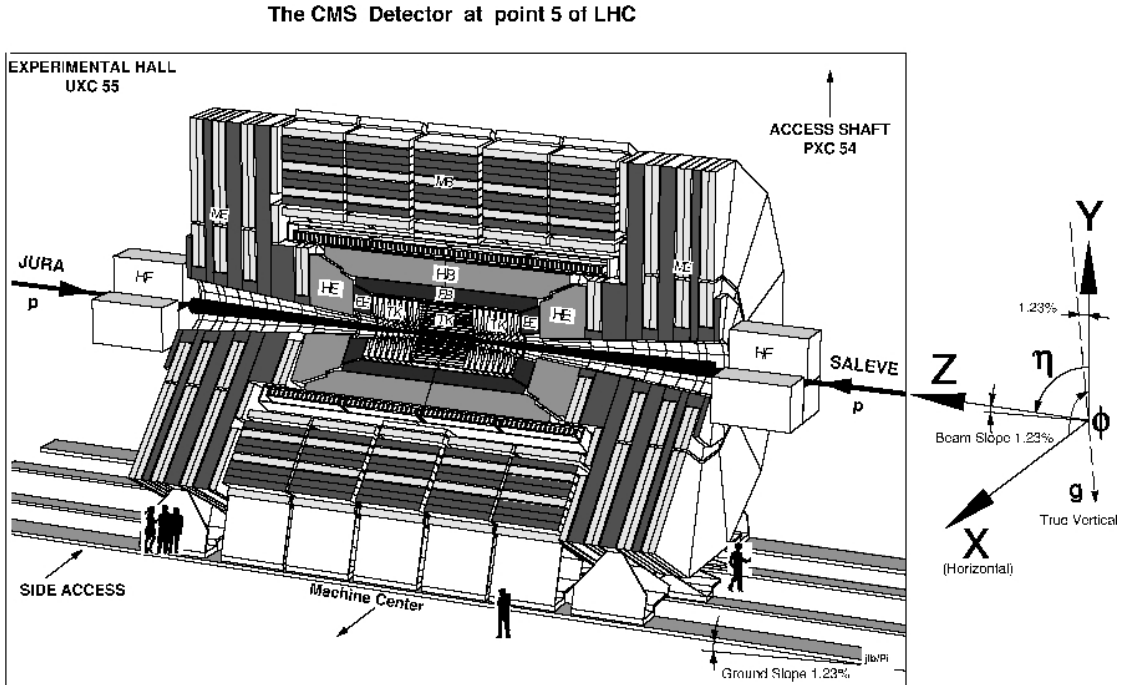


Figure 1.11: CMS coordinate system. ©CERN

200 We can also define two angles: the  $\phi$  angle in the x-y plane from the x-axis towards the  
 201 positive y-axis, and the  $\theta$  angle in the z-y plane from z-axis towards the positive y-axis.  
 202 In experimental particle physics is preferred to work with relativistic invariant quantities,  
 203 reason why instead of working with  $\theta$  we define the pseudorapidity  $\eta$ , equation 1.3.

$$\eta = -\ln \left( \tan \left( \frac{\theta}{2} \right) \right) \quad (1.3)$$

204 One can define another relativistic invariant quantity, the rapidity  $y$  as from equa-  
 205 tion 1.4. With  $\mathbf{p}$  being the momentum vector and  $E$  the energy of a given particle,  $p_L$   
 206 denotes its longitudinal component, that in our case is the same z-component.

$$y = \frac{1}{2} \ln \left( \frac{E + p_L}{E - p_L} \right) \quad (1.4)$$

207 On the limit that the mass of the particle is very small compared to its momentum,  
 208 one can replace approximate the particle energy by the momentum magnitude, giving  
 209 rise to the definition of the pseudorapidity in terms of the momentum of the particle  
 210  $\eta = \frac{1}{2} \ln \left( \frac{\mathbf{p} + p_L}{\mathbf{p} - p_L} \right)$

We define also the radial coordinate over the x-y plane, plane that is called the transverse plane being orthogonal to the longitudinal direction, the z-axis. In such plane are also defined the transverse quantities of particles, as the transverse momentum  $p_T$ . Finally, for any two objects an angular distance can be defined in the  $\eta - \phi$  plane, as in equation 1.5.

$$\Delta R = \sqrt{(\Delta\eta)^2 + (\Delta\phi)^2} \quad (1.5)$$

### 1.2.2 Magnet

In order to measure the momentum of the charged particles going inside the detector is crucial to apply the correct magnet field, sufficiently strong to bend very energetic particles. The momentum of a charged particle inside an uniform magnetic field can be written as

$$p = \gamma mv = qBr \quad (1.6)$$

where  $B$  is the magnitude of the magnetic field,  $\gamma$  the usual relativistic factor,  $m$  the mass of the particle,  $v$  its rapidity,  $q$  its charge and  $r$  the bending radius. The sagitta of the arc is

$$s = \frac{L^2}{8r} = \frac{qBL^2}{8p} \quad (1.7)$$

with  $L$  the distance the particle moved inside the magnetic filed. Inside a solenoid  $L$  is equal to the radius of it.

From relation 1.7 is possible to deduce that the resolution on the momentum of the particle has an inverse dependence with the magnetic field and the radius of the solenoid, as shown in equation 1.8. From there, for a better resolution is needed to increase the magnetic field and the radius of the solenoid.

$$\frac{dp}{p} \propto \frac{p}{BL^2} \quad (1.8)$$

The design of CMS magnet target both features, it utilizes a large solenoid of 6 m of diameter and 13 m long. It's made of 4 layers of windings of NbTi cable that is cooled to 4.45 K in order to achieve the superconducting state. This magnet is able to produce an uniform magnetic field inside of it of 3.8 T. Outside the magnet 5 wheels and 3 disks of iron are placed in order to return the flux of the magnetic field, inducing just a 2 T radial magnetic field outside the solenoid. This iron yoke contributes with most of the weight of the detector, 10000 tons. In between the iron yoke the muon chambers are placed.

### 1.2.3 Tracker system

The tracker system has been designed to specifically address the reconstruction of high  $p_T$  leptons, with particular interest in the isolation of electrons and, as a consequence, to

isolate photons. Also the tracker fulfill granularity requirements to reconstruct secondary vertexes to tag and reconstruct B-hadrons. The tracker system is able to reconstruct tracks of particles with at least 2 GeV of  $p_T$  with  $|\eta| < 2.5$ . Charged hadrons are reconstructed with an efficiency of at least 85% for  $p_T = 1$  GeV and up to 95% for  $p_T$  above 10 GeV. Another important point that was taken into account is the fact that the tracker is the part of CMS most exposed to radiation as it is the closest subsystem to the interaction point. The tracker system was built highly resistant to radiation damage and is expected to last for around 10 years. The pixel detector only lasts 2 years and was replaces during LS1.

The tracker has been built with three different technologies: Pixels, Silicon Strips and Micro Strip Gas Chambers (MSGCs). They are arranged concentrically in cylindrical volumes being the pixel detector the innermost and the MSGCs the outermost. The CMS tracker extends to a radius of 155 cm and a around 270 cm on each  $z$  direction. The pixel system is in the region with a radius below  $\approx 20$  cm, the silicon detector between  $\approx 20$  cm and  $\approx 60$  cm, and the MSGCs between  $\approx 70$  cm and  $\approx 120$  cm. The three subsystems are fast enough to work at 25 ns scale.

The pixel system is formed by three barrel layers and two end caps disks covering radii from 6 cm to 15 cm. It has an approximate active surface of one square meter with approximately  $40 \times 10^6$  channels with a cell size of 150  $\mu\text{m}$  by 150  $\mu\text{m}$ . This pixel system allows to obtain three highly precise points that are mainly used for reconstructing vertexes.

The Silicon Strip system is formed by a 5-layer barrel (TIB for Tracker Inner Barrel) and 10 disks (TID for Tracker Inner Disks) in each end cap. The strips length is 12.5 cm with a pitch from 61  $\mu\text{m}$  to 122  $\mu\text{m}$  for single-sided strips and for 81  $\mu\text{m}$  to 244  $\mu\text{m}$  for double-sided. It's able to achieve a hit resolution of about 15  $\mu\text{m}$ .

The MSGCs systems is composed of 6 layers in the barrel (TOB for Tracker Outer Barrel) and 11 disks in each end cap (TEC for Tracker EndCap, with a  $\pm$  sign depending on the  $z$  direction). Here the strips are 10 cm length for the inner layers and 25 cm for outer layers with a pitch from 200  $\mu\text{m}$  to 400  $\mu\text{m}$ , which gives a hit resolution of 35  $\mu\text{m}$  and 100  $\mu\text{m}$  respectively. The MSGCs and Silicon systems have an overall active area of around 300  $\text{m}^2$  with  $12 \times 10^6$  channels organized in more than ten thousand independent modules.

In figure 1.12 can be seen the disposition of all the tracker subsystems. From the design of the tracker system the best resolution on the  $p_T$  measurement is achieved in the  $|\eta| < 1.6$  region, this due to the presence of more layers of detector in the different subsystems, as shown in figure 1.13.

#### 1.2.4 Electromagnetic calorimeter

The CMS ECAL (Electromagnetic CALorimeter) is the detector subsystem designed to stop photons and electrons to measure their energy. It's an hermetic cylindrical calorimeter made of 61200 crystals in the barrel ( $|\eta| < 1.479$ ) and 7324 in each end cap ( $1.48 < |\eta| < 3$ ). The crystals material is lead-tungstate that is transparent, very dense (8.28 g/cm<sup>3</sup>), has a small Moliere radius (2.2 cm) and a short radiation depth

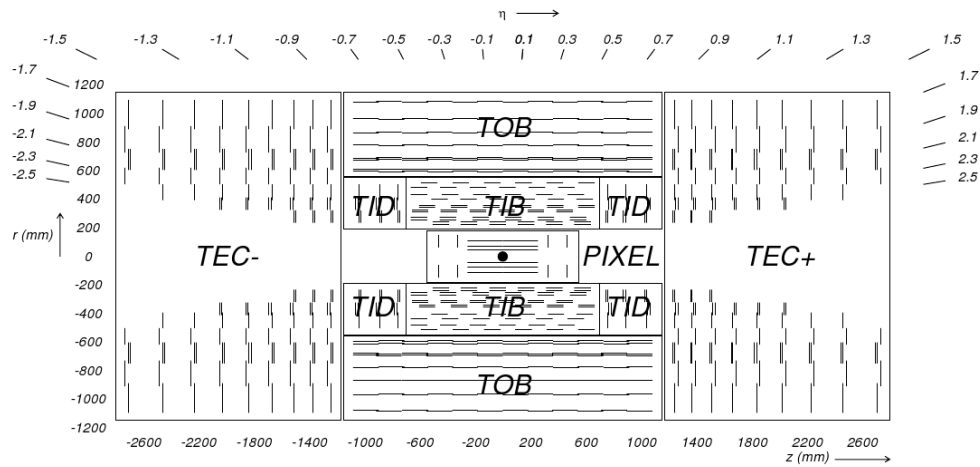
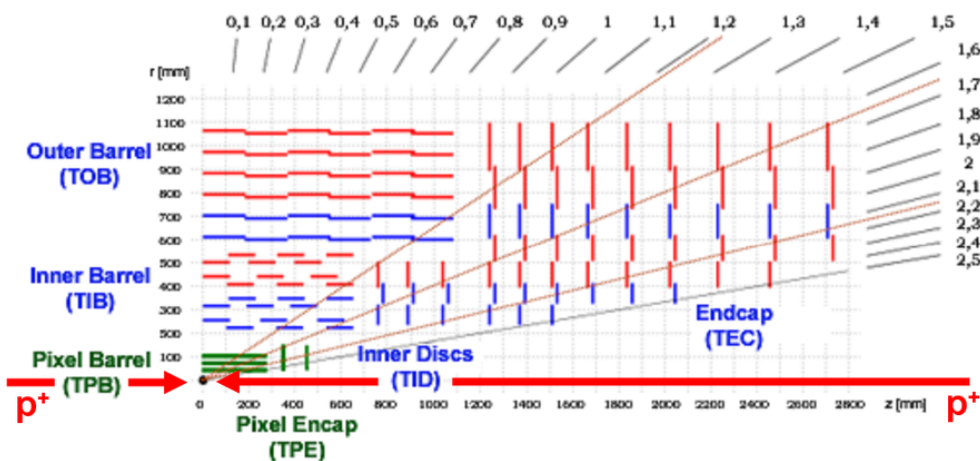


Figure 1.12: CMS tracker system configuration. ©CERN

Figure 1.13: Tracker resolution with  $\eta$ . ©CERN

( $X_0 = 0.89$  cm). This material has been chosen for the characteristics already described, but also because it is very fast emitting the scintillation light (in 25 ns), it has a very good energy resolution and resistance to radiation. The crystals are distributed in 36 supermodules, 1700 crystals each, in the barrel (EB for ECAL Barrel) and in four 'Dee's, of 3662 crystals each, in the end caps (EE for ECAL End cap). In the EB the scintillation light is collected by Avalanche Photo-Diodes, or APD, and by Vacuum Photo-Triodes, or VPT, in the EE. A preshower system is installed in face of each end cap to allow a better discrimination between photons and  $\pi^0$ 's. A representation of the CMS ECAL can be found on figure 1.14.

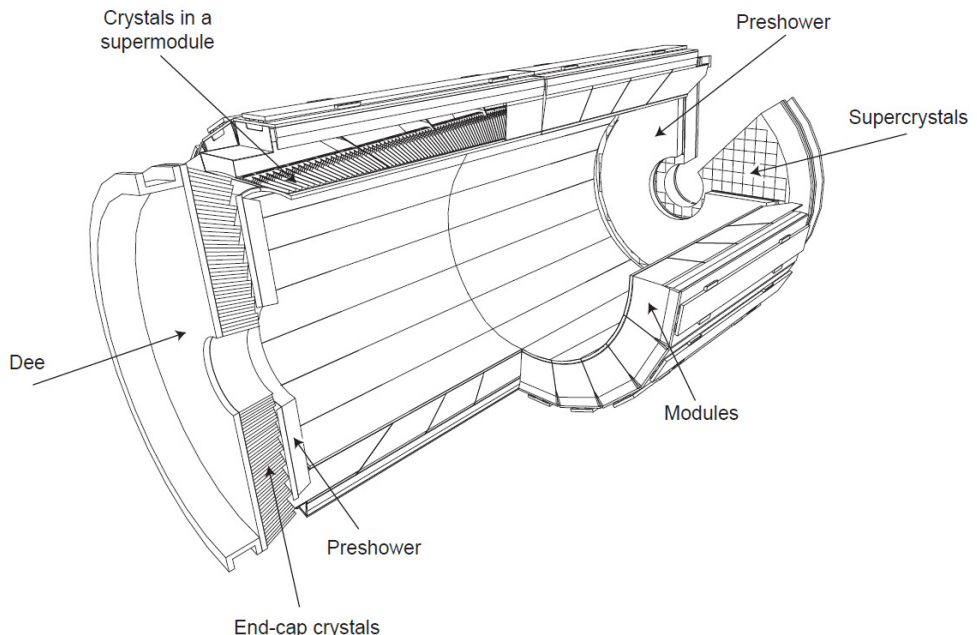


Figure 1.14: CMS ECAL representation. ©CERN

### 1.2.5 Hadronic Calorimeter

The CMS HCAL, for Hadronic CALorimeter, is the subdetector designed to measure the energy of hadrons produced in the collisions, mainly the neutral hadrons because the charged hadrons are already traced by the tracker. It's also designed to measure the missing energy coming from particles not being detected by any of the subsystems, as neutrinos. It's an hermetic set of subsystems covering up to  $|\eta| < 5.2$ :

- Hadron Barrel Calorimeter (HB): Covering  $|\eta| < 1.4$  is located between the ECAL barrel and the magnet.

- Hadron Endcap Calorimeter (HE): Extends the coverage of the barrel on the region  $1.4 < |\eta| < 3$ .
- Hadron Outer Calorimeter (HO): Located outside the magnet, uses it as an additional absorber.
- Hadron Forward Calorimeter (HF): Completes the coverage of the system from  $|\eta| = 3$  up to  $|\eta| = 5.2$ .

The CMS HCAL layout is shown in figure 1.15. The system is made of two parts, an absorber to develop the hadronic showers and a scintillator to measure the particles energy. The length scale of hadronic calorimetry is designated as the interaction length corresponding to the mean free path of an hadron in a material. The HB absorber is made of 40 mm thick steel plate, eight layers of brass plates of 50.5 mm thick, six brass plates of 56.5 mm thick and a steel plate of 75 mm thick. The HE uses the same absorber but with thicker plates, of 79 mm. Between the absorber plates a plastic scintillator, Kuraray SCSN81, of 3.7 mm thick is placed. In the region with  $|\eta| < 1.6$  the achieved granularity is  $\Delta\eta \times \Delta\phi = 0.087 \times 0.087$  and  $\Delta\eta \times \Delta\phi = 0.17 \times 0.17$  in the region with  $|\eta| > 1.6$ . This design gives a total of 70000 tiles used. The produced light in the HB is collected by optical fibers and transferred to the Hybrid Photo Diodes (HPDs). This diodes were chosen thanks to their small sensitivity to the magnetic field, an important feature due to the proximity of the HCAL to the magnet.

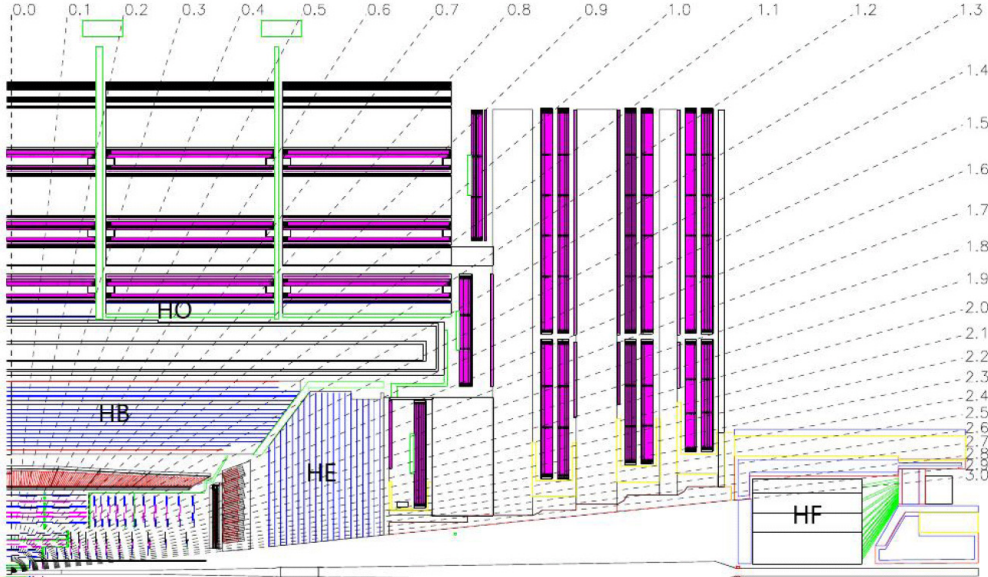


Figure 1.15: CMS HCAL representation. ©CERN

The HF design is very different from the rest of the HCAL subsystems. The most important challenge for the HF is the high resistance to radiation, while in the central

321 rapidity region 100 GeV are deposited in average in the forward region is 760 GeV.  
 322 For this reason it was chosen a Cherenkov detector made of quartz fibers with a steel  
 323 absorber. The light produced in the HF is collected by photo multipliers.

### 324 1.2.6 Muon chambers

325 The muon system of CMS is located at the most exterior layer of the detector due to  
 326 the penetration power of this particle. Muons are not stopped by the calorimeters and,  
 327 with neutrinos, they are able to escape the detector. The muon chambers are placed in  
 328 a cylinder around the HO and in disks on the end caps. Three main characteristics have  
 329 been fulfilled from the design: efficient muon identification, precision measurement of  
 330 muon charge and momentum and fast measurement to provide trigger capabilities. The  
 331 moun chambers are made of three different subsystems:

- 332 • Drift Tubes Chambers (DT): Located in the region with  $|\eta| < 1.2$  and disposed in  
 333 four layers. They consist of individual drift tubes of 50  $\mu\text{m}$  of diameter anode wire  
 334 with two electrode plates creating a drift electric field. The wall of the cell act as  
 335 cathode. The cells are filled with a gas mixture, 85% Argon and 15% CO<sub>2</sub>. The  
 336 tubes are organized in plaques that are also organized in SuperLayers (SL) each  
 337 one made of 4 plaques. The barrel is made of 250 DT's disposed in four cylinders  
 338 separated by iron yokes.
- 339 • Cathode Strip Chambers (CSC): Installed in the end caps, provide a coverage up  
 340 to  $|\eta| = 2.4$  from  $|\eta| = 0.9$ . These chambers are multi-wire proportional chambers  
 341 made of six planes of anode wires with 7 cathode planes. Four CSC stations  
 342 are placed in each end cap. The wires are oriented in azimuthal direction while  
 343 the cathode planes are radially oriented, allowing a complete measurement of the  
 344 position of the particle. This system is able to measure with a precision between  
 345 the 75  $\mu\text{m}$  and 150 $\mu\text{m}$ .
- 346 • Resistive Plate Chambers (RPC): This subsystem is made of gaseous parallel plate  
 347 detectors. This detector is specially useful for triggering as it is very fast and have  
 348 a good position resolution. There are 480 RPC distributed in 6 layers in the barrel  
 349 with the DT and in 3 layers in the end caps with the CSC, and covers the region  
 350 with  $|\eta| < 1.6$ .

351 On figure 1.16 can be found a representation of the muon system with the different  
 352 components. The DT and CSC system cover  $|\eta| < 2.4$  without any gap.

### 353 1.2.7 Trigger

354 LHC has been designed to provide experiments with proton-proton collisions every 25  
 355 ns, meaning a frequency of 40 MHz. Each recorded event by CMS has a nominal size  
 356 between 0.5 and 1 MB, what means a data flux of around 10<sup>9</sup> MB/s = 1PB/s that is  
 357 extremely big for transfer and for storing. Therefore, an on-line selection of events has

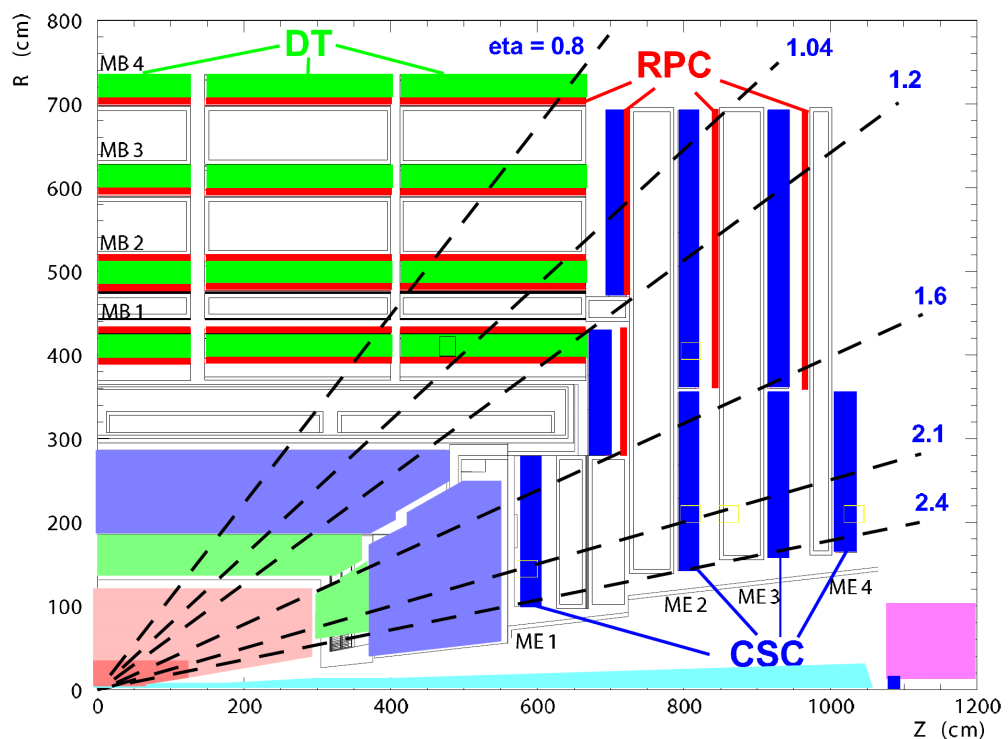


Figure 1.16: CMS muon chambers representation. ©CERN

358 to be done. The trigger system of CMS does this task in two fold, a level 1 (L1) and a  
 359 high level trigger (HLT). The L1 is hardware based and the HLT is software based.

360 From the searches conducted at CMS, the interesting events produced on proton-  
 361 proton collisions for new physics searches are very rare. The enormous majority of  
 362 events coming from proton-proton collisions correspond to well understood phenomena,  
 363 while new physics events are ‘exotic’ with regards to the most common type of events.  
 364 Then is interesting to keep only a part of the events, what actually eases the analysis  
 365 afterward done over the data.

366 The CMS trigger system is designed to keep only 100 kHz tops by the L1 and 300 Hz  
 367 by the HLT. L1 is reducing the data flux by 2 orders of magnitude and the HLT another  
 368 3 orders of magnitude.

### 369 **Level 1 trigger**

370 The L1 is designed to trigger over coarse data coming from the calorimeters and muon  
 371 chambers, holding data in pipe-lined memories in the front-end electronics. Therefore,  
 372 relies on very fast reconstruction of objects coming from this subsystems: muons,  
 373 electrons, photons, jets and missing energy. This reconstruction differs from the final  
 374 reconstruction of the objects, for example a jet for the L1 consists on successive energy  
 375 deposits in the ECAL and HCAL, while the off-line reconstruction take into account  
 376 also the tracker information.

377 The L1 starts from regional data coming from the subsystems which is afterward  
 378 combined in order to build ranked trigger objects in localized regions of the detector.  
 379 Global Muon and Calorimeter triggers sort the objects and send the best ranked to the  
 380 Global Trigger (GT). Before the GT no events are rejected, is only with the GT that  
 381 the selection is applied. The GT combines the information and can apply topological  
 382 requirements and take a decision on keeping or disregarding the event. On figure 1.17  
 383 can be found the work-flow of the L1.

384 The L1 cards are distributed between the detector and an adjoin cavern at 90 m  
 385 distance from the detector. The latency time L1 disposes between the collision and the  
 386 taking of the decision is about  $3.2 \mu\text{s}$ . Therefore, the front-end memory in the cards  
 387 should be able to keep in memory up to 128 bunch crossings.

### 388 **High Level Trigger**

389 The HLT take as input the events accepted by the L1 and process them using farms  
 390 of commercial processors. The HLT does additional operations on the selected events  
 391 making it much slower than L1 processing. In particular, the HLT takes also into account  
 392 the tracker information. Consequently, this system is able to take into consideration the  
 393 whole information of the detector. However, the reconstruction of objects done by the  
 394 HLT differs slightly from the final off-line reconstruction. The decision taking process  
 395 takes around 40 ms,  $10^4$  times more than for L1.

396 The events selected by HLT are finally stocked on disks under several paths depending  
 397 on the selection performed. There is a constant development of HLT paths focusing on

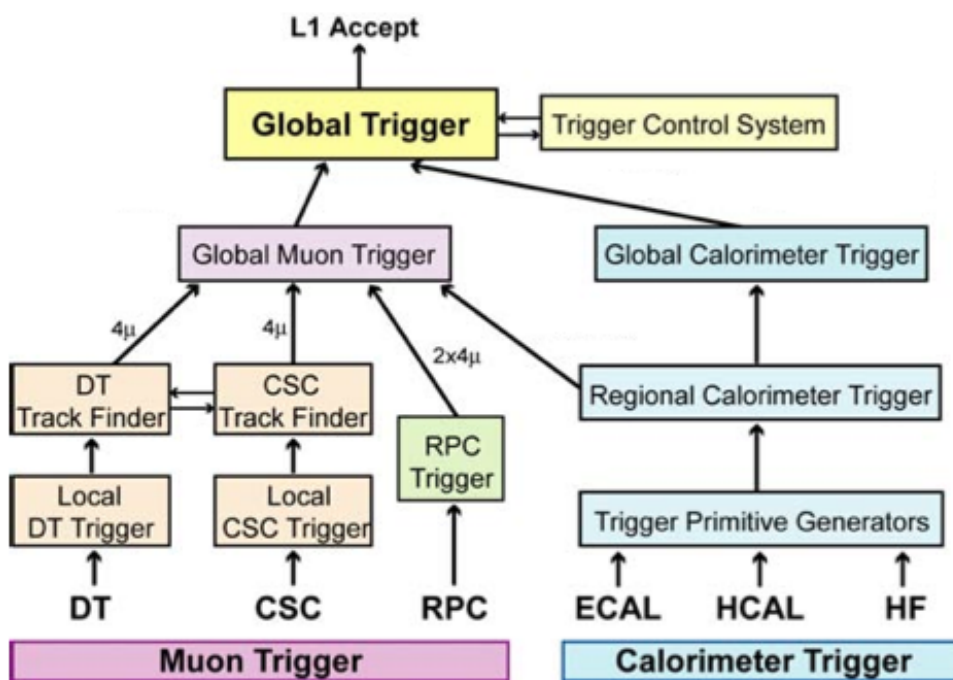


Figure 1.17: L1 architecture. ©CERN

<sup>398</sup> different analysis requirements in order to obtain the best possible selection efficiency  
<sup>399</sup> for specific signal types.

400 **Chapter 2**

401 **The Standard Model**

402 Since the Greeks, different theories about the composition and structure of the world  
403 have been formulated. At ancient Greece these theories were elaborated from a philo-  
404 sophical point of view. Nowadays, we count with a very sophisticated set of tools and  
405 concepts that allowed us to build up a general vision of nature, its components and  
406 structure. Moreover, on the subject of the constituents, or elemental constituents, we  
407 have developed a theory that is capable to describe the majority of known phenomena.  
408 This theory is the Standard Model (SM) of particle physics.

409 This SM relies in two of the more fancy constructs of modern physics and mathe-  
410 matics. From physics side, the quantum field theory; from mathematics, group theory.  
411 Quantum field theory has born from the understanding of processes that take place at  
412 very small spatial scales but in a regime where special relativity play an important role.  
413 To describe such, a major part of the most brilliant minds of the 20th century dedi-  
414 cated their life, Paul Dirac, Richard Feynman, Enrico Fermi among them. The theory  
415 of quantum fields has set in a common place two extraordinary achievements of physics:  
416 special relativity and quantum mechanics. With it we have been capable to describe  
417 many phenomena:  $\beta$  decay and  $\alpha$  decay, solid state, with many other.

418 From the mathematics side, group theory has become one of the most powerful tools  
419 for particle physicist. However, their development began quite early, with Galois around  
420 1830, and was used in other parts of physics, it's with Lie algebras and the possibility  
421 of describing continuous symmetries that the most important step will be given. Also,  
422 this would have not been possible with the amazing connection found by Emmy Noether  
423 in 1918. Her finding connected symmetries and physics in a form never known before.  
424 She found that for every conserved quantity in a system there is a symmetry followed  
425 by it. As group theory can be seen, in grosso modo, a way to mathematically describe  
426 symmetries, group theory became the tool to describe systems with conserved quantities.

427 In this chapter, we are going to present the basics of the SM. We describe its seminal  
428 ideas, its structure and content and its ultimate consequences. Finally, we close with its  
429 limitations.

## 430 2.1 Fields, symmetries and interactions

431 From the very beginning of physics, one of the most fundamental questions has been  
 432 how does bodies interact, and with it what exactly and interaction is. On the first type  
 433 of interaction ever studied by physics, gravity, Newton proposed the concept of distant  
 434 interaction, the idea that bodies could interact without being in direct contact. But the  
 435 question on how exactly that distant action was performed remained unanswered.

436 During the 19th and 20th century new phenomena were discovered pointing to  
 437 brand new interactions, electricity, magnetism, radioactivity and nuclear structure inside atoms.  
 438 The very precise and complete description of electromagnetism developed  
 439 by Gauss, Faraday, Ampère and finished by Maxwell arrived to the describe electricity  
 440 and magnetism under the formalism of only one interaction within the mathematical  
 441 formalism of classical fields. For the following discussion, and so on, we are going to  
 442 work in natural units for simplicity. In these units the speed of light  $c$  is normalized to  
 443 unity, as well as electron electric charge  $e$ , reduced Planck constant  $\hbar$  and Boltzmann  
 444 constant  $k_B$ . Then, masses and temperature are measured in energy units, i.e.  $eV$ , and  
 445 time and length in inverse energy units,  $eV^{-1}$ .

446 The definition of a classical field is an assignment of a quantity to every point in  
 447 space and time. For physics the quantity that is attributed it's a physical quantity such  
 448 as mass, electrical charge or probability. This quantity can be scalar or vector, giving  
 449 rise to the notion of scalar or vector field. As an example, a fluid can be described  
 450 in terms of fields, being the velocity of the fluid a vector field and its pressure a scalar  
 451 field. Generic classical electromagnetic interactions can be described with the help of one  
 452 vector field  $\vec{A}(x)$ , the vector potential, and one scalar field  $\phi(x)$ , the scalar potential.  
 453 In the formalism of four-vectors from relativistic dynamics one can organize this two  
 454 quantities in the four-potential  $A_\mu = (-\phi, \vec{A})$ . This can be used to define the strength  
 455 field tensor  $F_{\mu\nu} = \partial_\mu A_\nu - \partial_\nu A_\mu$ , where  $\partial_\mu = \left(-\frac{\partial}{\partial t}, \nabla\right)$  is the covariant derivative. From  
 456 the tensor is possible to obtain in a very generic and elegant way the equations of motion  
 457 of the free field using the Lagrangian formalism, as in equation 2.1. With the Lagrangian  
 458 density defined in equation 2.2.

$$\partial_\mu \left( \frac{\partial \mathcal{L}}{\partial(\partial_\mu A_\nu)} \right) - \frac{\partial \mathcal{L}}{\partial A_\nu} = 0 \quad (2.1)$$

$$\mathcal{L} = -\frac{1}{4} F^{\mu\nu} F_{\mu\nu} \quad (2.2)$$

459 It's very important to notice that the equations of motion of the free field are invariant  
 460 under the choice of the four-potential. More precisely, the covariant potential is not  
 461 unique and we can always add the covariant derivative of a scalar field,

$$A'_\mu = A_\mu + \partial_\mu \Lambda(x) \leftrightarrow \partial^\mu A'_\mu = 0 \quad (2.3)$$

462 and describe the same physics. This non-uniqueness corresponds to the choice of a zero-  
 463 point of the potential very well known in non-Lagrangian formalism of electrodynamics.

464 When we choose a specific value for this scalar field,  $\Lambda(x)$ , we say that the gauge has  
 465 been fixed.

466 One can also define a four current vector,  $J_\mu = (\rho, \vec{J})$  with  $\rho$  the electric charge  
 467 density and  $\vec{J}$  the current charge density. Then, plugging in the four current in the  
 468 Lagrangian of the free field, defined in equation 2.2,

$$\mathcal{L} = -\frac{1}{4}F^{\mu\nu}F_{\mu\nu} - A_\mu J^\mu \quad (2.4)$$

469 we can obtain the complete set of equations of motion of the field with charges and  
 470 currents.

471 The transformation stated from equation 2.3 can be understood as a transformation  
 472 of the field. These type of transformations are mathematically understood under the  
 473 group  $U(1)$ , where the generic transformation operator can be written as  $U = e^{i\theta(x)}$ .  
 474 It's said then that the electromagnetic vector potential is *invariant* under  $U(1)$   
 475 transformations. This property identifies an essential characteristic of electromagnetism, it's  
 476 symmetric behavior under  $U(1)$ .

477 From this reasoning the most interesting results are drawn when the same symmetry  
 478 is imposed to another fields. For example, considering a complex scalar field, the kinetic  
 479 Lagrangian is  $\mathcal{L} = (\partial^\mu\phi)^*\partial_\mu\phi$ . To apply the transformation is sufficient to apply the  
 480 operator as  $\phi' = U\phi$  and  $\phi^* = \phi U^{-1}$ . But it's evident that the Lagrangian is not the  
 481 same after applying such transformation. Then, in order to preserve the Lagrangian  
 482 under  $U(1)$  is necessary to change at the same time the derivative. Such transformation  
 483 is given in equation 2.5, where  $g$  is a constant.

$$\mathcal{D}^\mu = \partial^\mu - igA^\mu \quad (2.5)$$

484 Then, the proposed Lagrangian can be rewritten, including the vector field, as

$$\mathcal{L} = (\mathcal{D}^\mu\phi)^*\mathcal{D}_\mu\phi - \frac{1}{4}F^{\mu\nu}F_{\mu\nu} \quad (2.6)$$

485 that is invariant under  $U(1)$ . From the kinematic term with the new derivative interaction  
 486 terms between the scalar and the vector field can be derived, as  $igA^\mu\phi * \partial_\mu$ . This  
 487 shows that the requirement of the invariance under  $U(1)$  of the scalar field lead to the  
 488 introduction of an interaction with a vector field controlled by the constant  $g$ . We have  
 489 also seen that electromagnetic interaction is described precisely by a vector field and  
 490 that preserves  $U(1)$  symmetry. What implies that this symmetry is the connection to  
 491 electromagnetic interaction, practically identifying the interaction itself with the  $U(1)$   
 492 symmetry. In addition, using Noether theorem one can show that  $g$  is a conserved  
 493 quantity, as the electric charge.

494 But not only electromagnetism can be described via a continuous symmetry as  $U(1)$ .  
 495 On 1896 radioactivity was discovered by the french physicist Henri Becquerel. Three  
 496 years after, Marie and Pierre Curie studied in more detail the phenomenon and found  
 497 Polonium and Radium elements. And later on, Ernst Rutherford was able to describe  
 498 radioactivity as coming in three types, alpha ( $\alpha$ ), beta ( $\beta$ ) and gamma ( $\gamma$ ). He also

499 noticed that radioactivity was able to change matter, which allow him, with also other  
500 experiences, to propose an atomic model, describing elements as basically and external  
501 core of negative charges and a nucleus. Consequently, This findings implied the existence  
502 of interactions different to electromagnetism, acting at the atomic scale.

503 The interaction that undergoes radioactivity, beta decay, is called the weak interaction.  
504 In 1933 Enrico Fermi made a first theoretical description of this interaction, but  
505 only in 1968 Sheldon Glashow, Abdus Salam and Steven Weinberg were able to describe  
506 weak interaction with a symmetry group:  $SU(2)$ . Finally, the interaction that keeps the  
507 nucleus components together, the strong interaction, was described with  $SU(3)$  group  
508 mainly by Murray Gell-Mann in 1963.

509 There have been many attempts to describe gravity with the same formalism, but  
510 up to present such attempts have been unsuccessful. Such question remains one of the  
511 most important problems for modern particle physics.

## 512 **2.2 Quantum fields and particles**

513 Classical fields, introduced and described in last section 2.1, can be extended to a quan-  
514 tum theory. Such procedure is known as the quantization of fields and allow to unify  
515 special relativity and quantum mechanics in one theory, Quantum Field Theory (QFT),  
516 to describe the dynamics of systems in such regimes: rapidity close to the speed of light  
517 on the atomic or smaller scales.

### 518 **2.2.1 The mass problem**

### 519 **2.2.2 Spontaneous Symmetry Breaking**

### 520 **2.2.3 Higgs mechanism**

## 521 **2.3 Hierarchy problem and other limitations**

522 **Chapter 3**

523 **Vector Like Quarks: Generic  
model**

525 From chapter 2 we have seen how there are some parts in the SM that does not work very  
526 well. From such internal issues some further models/theories have been developed. All  
527 this theories are commonly grouped under the term Beyond Standard Model or simply  
528 BSM. One of the most famous BSM theory is supersymmetry (SUSY). This theory  
529 postulates a symmetry that does not distinguish between fermions and bosons. This idea  
530 have given birth to a plethora of model realizations and physics predictions. So far,  
531 nothing of the new consequences of this theory have been confirmed but the experiments  
532 have an enormous investment on their search. But not only SUSY have seen the day  
533 light, there is on the market an astonishing amount of BSM theories addressing different  
534 issues of the SM. Extra dimensions, fourth families, composite Higgs are a few of them.

535 In this chapter we will describe a bunch of models that introduce additional heavy  
536 quarks, heavier than the top, in order to solve the hierarchy problem, described on  
537 section 2.3.

538 **3.1 Motivation**

539 **3.2 Generic Formulation**

540 **3.3 Fesability study for a search of a  $T$  at LHC at 8 TeV**

541 **3.3.1 Production modes**

542 **3.3.2 Decay modes**

543 **3.3.3 Stragey for the full hadronic final state**

544 **3.3.4 Event selection**

545 **3.3.5 Results**



546 **Chapter 4**

547 **Understanding theory predictions  
548 via Monte-Carlo event generation**

549 However we have nowadays a very elegant and complete theoretical description of particle  
550 physics, is not always evident how to translate this theory in actual predictions, in actual  
551 measurements. Moreover, on the case of hadronic colliders, as the LHC, it's even more  
552 difficult due to the particularities of strong interaction. On this subject, a set of tools  
553 and approaches have been developed in order to be able to make accurate predictions  
554 from theory that could be directly researched for on the experiments, as CMS or ATLAS  
555 for example. In the present chapter, we describe such tools and formalisms and a set of  
556 studies comparing the well behavior of this tools with data.

557 **4.1 Mote-Carlo formalism**

558 **4.1.1 Partonic step**

559 **4.1.2 Hadronic step**

560 **4.1.3 Detector step**

561 **4.2 Tools**

562 **4.2.1 Matrix-element generators**

563 **4.2.2 Hadron generators**

564 **4.2.3 Detector simulation**

565 **4.3 Validation on data**



## <sup>566</sup> Chapter 5

### <sup>567</sup> **Search for a single produced T'** <sup>568</sup> **decaying into top and Higgs in** <sup>569</sup> **the full hadronic final state**

<sup>570</sup> In the present chapter we describe in full detail the search performed using 2012 data  
<sup>571</sup> collected by CMS for a T' in the full hadronic final state. The theoretical formalism for  
<sup>572</sup> such object has been described on chapter 3.

573 **5.1 Analysis Strategy**

574 **5.2 Datasets**

575 **5.3 Event selection**

576 **5.3.1 T' reconstruction with a  $\chi^2$  sorting algorithm**

577 **5.3.2 Efficiencies**

578 **Trigger**

579 **Selection**

580 **5.4 Background estimation from data**

581 **5.4.1 Known difficulties and tried methods**

582 **5.4.2 Method**

583 **5.4.3 Validation**

584 **5.5 Systematics**

585 **5.6 Results**

# <sup>586</sup> Bibliography

- <sup>587</sup> [1] O. S. Brüning, P. Collier, P. Lebrun, S. Myers, R. Ostojic, J. Poole, and  
<sup>588</sup> P. Proudlock, *LHC Design Report*. CERN, Geneva, 2004.
- <sup>589</sup> [2] **CMS Collaboration** Collaboration, G. L. Bayatian *et al.*, *CMS Physics:*  
<sup>590</sup> *Technical Design Report Volume 1: Detector Performance and Software*. Technical  
<sup>591</sup> Design Report CMS. CERN, Geneva, 2006. There is an error on cover due to a  
<sup>592</sup> technical problem for some items.
- <sup>593</sup> [3] **CMS Collaboration** Collaboration, G. L. Bayatian *et al.*, “CMS Physics:  
<sup>594</sup> Technical Design Report Volume 2: Physics Performance,” *J. Phys. G* **34**  
<sup>595</sup> no. CERN-LHCC-2006-021. CMS-TDR-8-2, (2007) 995–1579. 669 p. revised version  
<sup>596</sup> submitted on 2006-09-22 17:44:47.
- <sup>597</sup> [4] **ATLAS Collaboration** Collaboration, A. Collaboration, *ATLAS detector and*  
<sup>598</sup> *physics performance: Technical Design Report*. Technical Design Report ATLAS.  
<sup>599</sup> CERN, Geneva, 1999. Electronic version not available.
- <sup>600</sup> [5] **LHCb Collaboration** Collaboration, J. Alves, A. Augusto *et al.*, “The LHCb  
<sup>601</sup> Detector at the LHC,” *JINST* **3** (2008) S08005.
- <sup>602</sup> [6] **ALICE Collaboration** Collaboration, P. Cortese, C. W. Fabjan, L. Riccati,  
<sup>603</sup> K. Safarik, and H. de Groot, *ALICE physics performance: Technical Design*  
<sup>604</sup> *Report*. Technical Design Report ALICE. CERN, Geneva, 2005. revised version  
<sup>605</sup> submitted on 2006-05-29 15:15:40.
- <sup>606</sup> [7] **UA4/2 Collaboration** Collaboration, C. Augier *et al.*, “Predictions on the total  
<sup>607</sup> cross-section and real part at LHC and SSC,” *Phys.Lett.* **B315** (1993) 503–506.



# **608** Contents

<b>609</b>	<b>1</b>	<b>The CMS experiment at LHC</b>	<b>3</b>
610	1.1	The Large Hadron Collider . . . . .	3
611	1.1.1	Injector chain . . . . .	4
612	1.1.2	Main ring . . . . .	4
613	1.1.3	Run 1 . . . . .	8
614	1.1.4	Other experiments at LHC . . . . .	10
615	1.2	The Compact Muon Solenoid experiment . . . . .	11
616	1.2.1	Coordinate system . . . . .	13
617	1.2.2	Magnet . . . . .	15
618	1.2.3	Tracker system . . . . .	15
619	1.2.4	Electromagnetic calorimeter . . . . .	16
620	1.2.5	Hadronic Calorimeter . . . . .	18
621	1.2.6	Muon chambers . . . . .	20
622	1.2.7	Trigger . . . . .	20
<b>623</b>	<b>2</b>	<b>The Standard Model</b>	<b>25</b>
624	2.1	Fields, symmetries and interactions . . . . .	26
625	2.2	Quantum fields and particles . . . . .	28
626	2.2.1	The mass problem . . . . .	28
627	2.2.2	Spontaneous Symmetry Breaking . . . . .	28
628	2.2.3	Higgs mechanism . . . . .	28
629	2.3	Hierarchy problem and other limitations . . . . .	28
<b>630</b>	<b>3</b>	<b>VLQ models</b>	<b>29</b>
631	3.1	Motivation . . . . .	29
632	3.2	Generic Formulation . . . . .	29
633	3.3	Fesability study for a search of a $T$ at LHC at 8 TeV . . . . .	29
634	3.3.1	Production modes . . . . .	29
635	3.3.2	Decay modes . . . . .	29
636	3.3.3	Stragey for the full hadronic final state . . . . .	29
637	3.3.4	Event selection . . . . .	29
638	3.3.5	Results . . . . .	29

639	<b>4 MC event generation</b>	<b>31</b>
640	4.1 Mote-Carlo formalism . . . . .	31
641	4.1.1 Partonic step . . . . .	31
642	4.1.2 Hadronic step . . . . .	31
643	4.1.3 Detector step . . . . .	31
644	4.2 Tools . . . . .	31
645	4.2.1 Matrix-element generators . . . . .	31
646	4.2.2 Hadron generators . . . . .	31
647	4.2.3 Detector simulation . . . . .	31
648	4.3 Validation on data . . . . .	31
649	<b>5 Single VLQ search</b>	<b>33</b>
650	5.1 Analysis Strategy . . . . .	34
651	5.2 Datasets . . . . .	34
652	5.3 Event selection . . . . .	34
653	5.3.1 T' reconstruction with a $\chi^2$ sorting algorithm . . . . .	34
654	5.3.2 Efficiencies . . . . .	34
655	5.4 Background estimation from data . . . . .	34
656	5.4.1 Known difficulties and tried methods . . . . .	34
657	5.4.2 Method . . . . .	34
658	5.4.3 Validation . . . . .	34
659	5.5 Systematics . . . . .	34
660	5.6 Results . . . . .	34